NONLINEAR DYNAMIC INTERTWINING OF RODS WITH SELF-CONTACT

(accepted for publication in International Journal of Non-Linear Mechanics, 2007)

AUTHORS:

Sachin Goyal[1] (sgoyal@whoi.edu)

N. C. Perkins[2] (ncp@umich.edu) – Corresponding Author

Christopher L. Lee[3] (christopher.lee@olin.edu)

AFFILIATIONS:

[1]Applied Ocean Physics and Engineering

Woods Hole Oceanographic Institution, Woods Hole MA 02543 (U.S.A.)

[2]Department of Mechanical Engineering

University of Michigan, Ann Arbor MI 48109 (U.S.A.)

[3]Department of Mechanical Engineering

Olin College, Needham, MA 02492 (U.S.A.)

ABSTRACT

Twisted marine cables on the sea floor can form highly contorted three-dimensional loops that resemble tangles. Such tangles or ‘hockles’ are topologically equivalent to the plectomenes that form in supercoiled DNA molecules. The dynamic evolution of these intertwined loops is studied herein using a computational rod model that explicitly accounts for dynamic self-contact. Numerical solutions are presented for an illustrative example of a long rod subjected to increasing twist at one end. The solutions reveal the dynamic evolution of the rod from an initially straight state, through a buckled state in the approximate form of a helix, through the dynamic collapse of this helix into a near-planar loop with one site of self-contact, and the subsequent intertwining of this loop with multiple sites of self-contact. This evolution is controlled by the dynamic conversion of torsional strain energy to bending strain energy or, alternatively by the dynamic conversion of twist (Tw) to writhe (Wr).

KEY WORDS

Rod Dynamics, Self-contact, Intertwining, DNA Supercoiling, Cable Hockling

1. INTRODUCTION

Cables laid upon the sea floor may form loops and tangles as illustrated in Fig. 1. The loops, sometimes referred to as *hockles*, may cause localized damage and, in the case of fiber optic cables, may also prevent signal transmission. These highly nonlinear deformations are initiated by a combination of low tension or compression (i.e. cable *slack*) and residual torsion sufficient to induce torsional buckling of the cable. Tangles evolve from a subsequent dynamic collapse of the buckled cable into highly nonlinear and intertwined configurations with self-contact.

The looped and tangled forms of marine cables are topologically equivalent to the 'plectonemic supercoiling' of long DNA molecules as illustrated in Fig. 2 (refer to [1, 2]). Figure 2 depicts a DNA molecule on three different length scales as reproduced from [3, 4]. The smallest length scale (far left) shows a segment of the familiar 'double-helix' which has a diameter of approximately 2 nanometers (nm). One complete helical turn is depicted here and this extends over a length of approximately 3 nm.

On an intermediate spatial scale (middle of Fig. 2), the double helix now appears as a long and slender DNA molecule that might be realized when considering tens to hundreds of helical turns (approximately tens to hundreds of nm). Two idealized 'long-length scale structures' of DNA are illustrated to the far right in Fig. 2. Here, the exceedingly long DNA molecule may contain thousands to millions of helical turns and behave as a very flexible filament with lengths ranging from micron to millimeter scales

or even longer. The long-length scale curving and twisting of this flexible molecule is referred to as *supercoiling*. Two generic types of supercoils are illustrated. A *plectonemic supercoil* leads to an interwound structure where the molecule wraps upon itself with many sites of apparent 'self-contact'. By contrast, a *solenoidal supercoil* possesses no self-contact and forms a secondary helical structure resembling a coiled spring or a telephone cord.

Often with the aid of proteins, DNA must supercoil for several key reasons. First, supercoiling provides an organized means to compact the very long molecule (by as much as 10^5) within the small confines of the cell nucleus. An unorganized compaction would hopelessly tangle the molecule and render it useless as the medium for storing genetic information. Second, supercoiling plays important roles in the transcription, regulation and repair of genes. For instance, specific regulatory proteins are known to aid or to hinder the formation of simple loops of DNA which in turn regulate gene activity; refer, for example, to Schleif [5] and Semsey et al. [6].

Like the tangling of marine cables above, the intertwining of DNA is inherently a nonlinear dynamic process controlled by structural properties (e.g., elasticity) and applied forces (e.g., protein interactions). Rod theory provides a useful framework to explore the dynamics of intertwining of long filament-like structures such as cables and DNA molecules, as described, for example in Goyal [7]. The mechanics of intertwining immediately invokes formulations for self-contact in rod theory which remain a significant challenge as emphasized recently in [8, 9].

The inclusion of self-contact in *equilibrium* formulations of rod theory has been treated in [8-16]. In particular, Chouaieb et al. [8] evaluate helical equilibria where self-contact is accounted for by imposing bounds on helical curvature and torsion. The formation of self-contact in the equilibria generated from 'closed' or 'circular' rods (e.g., representative of DNA plasmids) is examined in Coleman et al. [12, 14-16] using numerical energy minimization. The mathematical existence of such solutions is deduced in Gonzales et al. [13] by careful formulation of the geometric excluded volume constraint on self-intersection. The excluded volume constraint is formulated in terms of rod centerline curvature in Schuricht and Mosel [10] and appended via Lagrange multiplier to the Euler-Lagrange equation for rod equilibrium with self-contact. The analysis of 'open' rods (e.g., rods that do not close upon themselves) requires consideration of two sets of boundary conditions through which loads may also be applied. A numerical study of the self-contacting equilibria of 'open' rods reveals the bifurcations generated by varying compression or tension and twist applied at the boundaries; refer to Coleman et al. [16] and Heijden et al. [11]. A recent extension in Heijden et al. [9] considers cases where the rod is constrained to lie on the surface of a cylinder. Open questions regarding the analysis of rods with self-contact are emphasized in Heijden et al. [9] by the lament "*We are still far from understanding analytically the solutions of the Euler-Lagrange equations for general contact situations. Even if we limit ourselves to global minimizers of an appropriate energy functional, we can prove little about the form of solutions as soon as contact is taken into account.*"

In contrast to the equilibrium formulations above, very few *dynamical* formulations of rod theory have been proposed that incorporate self-contact. Nevertheless, such formulations enable one to explore the dynamic evolution of self-contacting states and possible dynamic transitions between them. For instance, the slow twisting of the filament treated in Goyal et al. [17] ultimately induces a sudden dynamic collapse of an intermediate helical loop into an intertwined form. An approximate dynamical formulation is also presented in Klapper [18] where inertial effects are ignored in favor of dissipation and stiffness effects.

In this paper, we revisit the slow twisting of a filament [17] with the objective to develop a fundamental understanding of the dynamic evolution of its intertwined states. In particular, we describe how intertwined states result from a sudden collapse of helically-looped states through a rapid conversion of torsional to bending strain energy. The remainder of this paper is organized as follows. Sections 2 and 3 summarize a computational dynamic rod model that incorporates self-contact (refer to Goyal [7]). Section 4 presents an illustrative example of a non-homogeneous rod subject to pure torsion. Results highlight the dynamic evolution from straight to looped to intertwined states following a dramatic collapse to self-contact. We close in Section 5 with conclusions.

2. COMPUTATIONAL ROD MODEL – A SUMMARY

The rod segment illustrated in Fig. 3 is a thin (1-dimensional) element that may undergo two-axis bending and torsion in forming a three-dimensional space curve. This curve represents the rod centerline which, in the context of double-stranded DNA, represents the helical axis of the duplex. We develop the dynamical model by employing the classical approximations of Kirchhoff and Clebsch [19] as detailed in Goyal [7]. A summary is provided here.

2.1 Rod Kinematics, Constitutive Law, and Energy

Consider the infinitesimal element of a Kirchhoff rod shown in Fig. 3. The three-dimensional curve $R(s,t)$ formed by the centerline is parameterized by the arc length coordinate s and time t. The body-fixed frame $\{a_i\}$ at each cross-section is employed to describe the orientation of the cross-section with respect to the inertial frame $\{e_i\}$. The angular velocity $\omega(s,t)$ of the cross-section is defined as the rotation of the body-fixed frame $\{a_i\}$ per unit time relative to the inertial frame $\{e_i\}$ and satisfies

$$\left(\frac{\partial a_i}{\partial t}\right)_{\{e_i\}} = \omega \times a_i, \tag{1}$$

where the subscript specifies the reference frame relative to which the derivative has been taken. We also define a 'curvature and twist vector' $\kappa(s,t)$ as the rotation of the body-fixed frame $\{a_i\}$ per unit arc length relative to the inertial frame $\{e_i\}$ which satisfies

$$\left(\frac{\partial a_i}{\partial s}\right)_{\{e_i\}} = \kappa \times a_i. \tag{2}$$

In a stress-free state, the rod conforms to its natural geometry defined by $\kappa_0(s)$. The difference $\{\kappa(s,t)-\kappa_0(s)\}$ results in an internal moment $q(s,t)$ at each cross-section of the rod. The relationship between the change in curvature/twist $\{\kappa(s,t)-\kappa_0(s)\}$ and the restoring moment $q(s,t)$ is governed by a constitutive law for bending and torsion. While many generalizations of the constitutive law are discussed in Goyal [7], in this study we employ the linear elastic law

$$q(s,t) = B(s)(\kappa(s,t)-\kappa_0(s)) \tag{3}$$

where $B(s)$ is a positive definite stiffness tensor that is a prescribed function of position *s*. As demonstrated in carefully controlled, laboratory-scale tests by Heijden et al. [11], the linear elastic material law assumed above is capable of capturing the bifurcation behaviors responsible for the looping and intertwining of thin rods. While these experiments were conducted using one type of material (nickel titanium alloy nitinol), other applications may require the specification of nonlinear material laws. Such generalizations can be readily accounted for in the formulation discussed in Goyal [7]. The resulting strain energy density is therefore

$$S_e(s,t) = \frac{1}{2}(\kappa(s,t)-\kappa_0(s))^T B(s)(\kappa(s,t)-\kappa_0(s)). \tag{4}$$

We further employ a diagonalized form of $B(s)$ by choosing $\{a_i\}$ to coincide with the 'principal torsion-flexure axes' of the cross-section (refer to Love [19]). In particular, a_1 and a_2 are in the plane of the cross-section and are aligned with the principal flexure axes while a_3 is normal to the cross-section and coincides with the tangent $\hat{t}$. The resulting diagonal form of the stiffness tensor $B(s)$ is

$$B(s) = \begin{bmatrix} A_1(s) & 0 & 0 \\ 0 & A_2(s) & 0 \\ 0 & 0 & C(s) \end{bmatrix}, \tag{5}$$

where $A_1(s)$ and $A_2(s)$ are bending stiffnesses about the principal flexure axes along a_1 and a_2 respectively, and $C(s)$ is the torsional stiffness about principal torsional or 'tangent' axis a_3. Furthermore, in the results that follow, the rod is assumed to be isotropic[1] but non-homogeneous (i.e. $A_1(s) = A_2(s) = A(s)$). The resultant of the stress-distribution at any cross-section not only results in a net internal moment $q(s,t)$, but also net tensile and shear forces $f(s,t)$ which remain unknowns in this formulation.

The kinetic energy of the rod depends upon the centerline velocity $v(s,t)$ and the cross-section angular velocity $\omega(s,t)$. Let $m(s)$ denote the mass of the rod per unit arc length and $I(s)$ denote the tensor of principal mass moments of inertia per unit arc length. Then the rod kinetic energy density is

[1] The rod is assumed to have circular cross section in this study with axi-symmetric bending stiffness.

$$K_e(s,t) = \frac{1}{2}\omega(s,t)^T I(s)\omega(s,t) + \frac{1}{2}v(s,t)^T m(s)v(s,t)\,. \tag{6}$$

We choose the vectors $v(s,t)$, $\omega(s,t)$, $\kappa(s,t)$ and $f(s,t)$ as four unknown field variables in the formulation below. The kinematical quantities $\kappa(s,t)$, $\omega(s,t)$ and $v(s,t)$ can be readily integrated to compute the rod configuration $R(s,t)$ and the cross-section orientation as given by $\{a_i(s,t)\}$; refer to Fig. 3 and to Goyal [7].

Depending upon the application, the rod may also interact with numerous external field forces including those produced by gravity, a surrounding fluid medium, electrostatic forces, contact with other bodies or with the rod itself, , etc. The resultant of these external forces and moments per unit length is denoted by $F(s,t,...)$ and $Q(s,t,...)$, respectively. In general, these quantities may be functionally-dependent on the kinematical quantities $\kappa(s,t)$, $\omega(s,t)$ and $v(s,t)$ in addition to the rod configuration $R(s,t)$.

We next specify the four field equations required to solve for the four vector unknowns $\{v,\omega,\kappa,f\}$. In the field equations, we employ partial derivatives of all quantities relative to the body-fixed frame $\{a_i\}$ and recall the following relations to the partial derivatives relative to the inertial frame for a vector quantity υ (refer to Greenwood [20]):

$$\left(\frac{\partial \upsilon}{\partial t}\right)_{\{a_i\}} = \left(\frac{\partial \upsilon}{\partial t}\right)_{\{e_i\}} - \omega\times\upsilon \quad \text{and} \quad \left(\frac{\partial \upsilon}{\partial s}\right)_{\{a_i\}} = \left(\frac{\partial \upsilon}{\partial s}\right)_{\{e_i\}} - \kappa\times\upsilon, \tag{7}$$

For notational convenience, henceforth, we drop the subscript for the body-fixed frame.

2.2 Equations of Motion

The balance law for linear momentum of the infinitesimal element shown in Fig. 3 becomes

$$\frac{\partial f}{\partial s} + \kappa \times f = m\left(\frac{\partial v}{\partial t} + \omega \times v\right) - F \tag{8}$$

and that for angular momentum becomes

$$\frac{\partial q}{\partial s} + \kappa \times q = I\frac{\partial \omega}{\partial t} + \omega \times I\omega + f \times \hat{t} - Q\,, \tag{9}$$

Here, $\hat{t}(s,t)$ is the unit tangent vector along the centerline (directed towards increasing arc length s) and the internal moment $q(s,t) = B(s)(\kappa(s,t) - \kappa_0(s))$ upon substitution of the constitutive law Eq. (3).

2.3 Constraints and Summary

The above formulation is completed with the addition of two vector constraints. The first enforces *inextensibility* and *unshearability* which take the form

$$\frac{\partial v}{\partial s} + \kappa \times v = \omega \times \hat{t} \,. \tag{10}$$

The second follows from continuity requirements for ω and κ in the form of the *compatibility* constraint

$$\frac{\partial \omega}{\partial s} + \kappa \times \omega = \frac{\partial \kappa}{\partial t} \,. \tag{11}$$

Detailed derivations of these constraints are provided in Goyal [7].

The four vector equations Eq. (8-11) in the four vector unknowns $\{v, \omega, \kappa, f\}$ result in a 12^{th} order system of nonlinear partial differential equations in space and time. They are compactly written as

$$M(Y,s,t)\frac{\partial Y}{\partial t} + K(Y,s,t)\frac{\partial Y}{\partial s} + \mathbb{F}(Y,s,t) = 0 \tag{12}$$

where $Y(s,t) = \{v, \omega, \kappa, f\}$ and the operators M , K and $\mathbb{F}$ are described in Goyal et al. [7, 21]. These equations are not integrable in general and thus we pursue a numerical solution as detailed in Goyal et al. [7, 21]. In particular, we discretize the equations above by employing a finite difference algorithm using the generalized-α method (refer to Chung and Hulbert [22]) in both space and time. Doing so yields a method that is unconditionally stable and second-order accurate. A single numerical parameter can be varied to control maximum numerical dissipation. The difference equations so obtained are implicit and their solution must satisfy the rod boundary conditions. The boundary

conditions are satisfied using a shooting method in conjunction with Newton-Raphson iteration. In addition, this formulation also incorporates the forces generated by self-contact which, being central to the objective of this paper, we describe in some detail below.

3. NUMERICAL FORMULATION OF DYNAMIC SELF-CONTACT

A numerical formulation of self-contact begins with first determining the likely sites where self-contact exists or will soon occur. An efficient search strategy for these sites [7] is as follows. Consider two remote segments of the discretized rod that are approaching contact as shown in Fig. 4. The lower segment contains three spatial grid points denoted as 1, 2 and 3 while the upper segment contains one grid point denoted as 4. Grid point 4 is likely to interact with the grid point 2 as the two segments approach each other. We introduce a *screening aperture* of angle θ formed by a pair of conical surfaces centered at each grid point (illustrated at grid point 2 in Fig. 4). We use this aperture to efficiently search for only those points that may potentially interact through self-contact. This aperture specifically excludes non-physical 'contact' forces between nearby grid points on the same segment (such as 1, 2 and 3 in lower segment). The aperture reduces to the plane of the rod cross-section as $\theta \rightarrow 0°$, and it expands to the entire space as $\theta \rightarrow 180°$.

During simulation, the separation d between each pair of grid points is measured. A repulsive (contact) force is introduced between these grid points only if two

conditions are met: 1) the distance d is less than a specified tolerance, and 2) the two grid points lie within each other's *screening aperture*. This search strategy ensures that the contact forces are approximately normal to the rod surfaces and also allows for sliding contact. The interaction force can in general be a function of d and $\dot{d}$ (the approach speed) and it is included in the balance of linear momentum Eq. (8) through the distributed force term F. Example interaction laws that can be employed include (attractive-repulsive) Lennard-Jones type (refer to, for example Schlick et al. [23]), (screened repulsion) Debye-Huckle type (refer to, for example Schlick et al. [24]), general inverse-power laws (refer to, for example Klapper [18]), and idealized contact laws for two solids (refer to, for example Heijden et al. [11] and Coleman et al. [12]). In the specific case of DNA, one might introduce a fictitious charged and cylindrical surface that circumscribes the molecule to capture the repulsive effects of the negatively charged backbone.

4. RESULTS

The computational model above is used to explore the dynamic evolution of an intertwined state induced by slowly increasing the twist applied to one end of an elastic rod. The numerical solutions reveal three major behaviors: 1) the torsional buckling of an initially straight rod into the approximate shape of a helix, 2) the dramatic collapse of this helix to a near-planar loop with self-contact at a single point, and 3) the subsequent intertwining of the loop with multiple sites of self-contact.

4.1 Illustrative Example

Figure 5 defines an illustrative example which consists of an initially straight, linearly elastic rod subjected to monotonically increasing twist at the right end at $s = 0$. This end cannot move and it is otherwise constrained in rotation (no rotation about the principal axes a_1 and a_2). The left end at $s = L$ is fully restrained in rotation and cannot translate in the transverse (a_1-a_2) plane. This end, however, may translate along the e_2 axis. Constraining the ends in rotation conserves the number of twisting turns added to the rod which is equivalent to conserving the topological invariant called the 'linking number' defined in Section 4.4. By contrast, having any rotational freedom at any end might allow the rod to swivel at that end releasing the linking number and resulting in distinctly different behavior. An insightful discussion of these and other boundary conditions is provided in [11].

The material and geometric parameters that define the example are listed in Table 1 together with basic discretization parameters used in the numerical algorithm; refer to Goyal et al. [7, 21] for a complete description of the numerical parameters. The example rod has a circular cross-section which varies along its length. In particular, the central portion of the rod (middle 25%) is necked down to a smaller diameter that is 10% smaller than the end regions. We have chosen this non-homogenous rod to illustrate both the

generality of the computational model as well as to promote torsional buckling and subsequent intertwining within the ('softer') central portion. The small 10% reduction in the diameter produces a significant (≈ 35%) reduction in torsional stiffness ($C(s) = GJ_3$) and bending stiffness ($A(s) = EJ_{1,2}$) in the central portion.

As a representative law for self-contact, we choose for this example the following form for the repulsive force

$$\left|F_{contact}\right| = \rho_c A_c \left(\frac{k_1}{(d - 0.5D)^{k_2}} + \frac{k_3}{d} \dot{d} \left|\dot{d}\right|^{k_4} \right), \tag{13}$$

with example parameters: $k_1 = 10^{-7}\text{m}^4/\text{s}^2$, $k_2 = 3$, $k_3 = 10^{-6}$ and $k_4 = 1$. This contact law is one of many possible that capture both nonlinear repulsion and dissipation. This example contact law retains an inverse power dependence on the separation parameter (*d-0.5D)* common to (the repulsive part of) the Lennard-Jones and Debye-Huckle formulations as well as a similar inverse power law employed in [18]. The results that follow are rather insensitive to changes in the specific parameter values selected above. However, the stability of the numerical algorithm is sensitive to the functional form of the contact law for the following reason. As will be seen in the examples, the first approach to self-contact follows from a dramatic dynamic collapse to contact and thus the contact force can build very rapidly. The addition of dissipation in (13), which does not alter the steady-state prediction of the looped and intertwined states, helps stabilize the numerical algorithm by limiting the otherwise destabilizing growth of the contact force.

In addition to the contact law above, the only other body force considered is a dissipative force. As one example, we introduce the viscous drag imparted by a surrounding fluid environment in the form of the standard Morison drag law [25]. This distributed drag, which manifests itself in the balance of linear momentum Eq. (8) through the distributed force term F, is computed as [21]:

$$F_{drag} = -\frac{1}{2}\rho_f D\left\{C_n\left|v\times\hat{t}\right|\hat{t}\times\left(v\times\hat{t}\right)+\pi C_t\left(v\cdot\hat{t}\right)\left|v\cdot\hat{t}\right|\hat{t}\right\}, \tag{14}$$

Here, C_n is the normal (form) drag coefficient, C_t is the tangential (skin friction) drag coefficient, and ρ_f is fluid density. Example values of these parameters are reported in Table 1.

Any form of fluid and material dissipation would tend to slow the dynamic collapse of the helically deformed rod into a loop with self-contact. Therefore, any quantitative prediction of the time scale of this collapse (e.g., for a cable in the ocean environment, or DNA in a biological buffer) would first require an accurate characterization of the relevant dissipation mechanisms. In our example, we chose a Morison drag law to demonstrate how one may incorporate realistic hydrodynamic drag in the context of an oceanographic cable.

4.2 Evolution of Self-Contact and Intertwining

By increasing the rotation (twist) slowly at the right end, the internal torque eventually reaches the bifurcation condition associated with the classical torsional buckling of a

straight rod (refer to Zachmann [26]). This rotation is generated by prescribing the angular velocity component ω_3 at the right end as shown in Fig. 6 (not to scale). In addition, the left end is allowed to translate freely during the first 30 seconds and is then held fixed to control what would otherwise be an exceedingly rapid collapse to self-contact as described in the following.

As the right end is initially twisted by a modest amount, the rod remains straight. There is an abrupt change however when the twist reaches the bifurcation value associated with the Zachmann buckling condition [26] and the straight (trivial) configuration becomes unstable. This occurs at approximately 16 seconds in this example. The computational model captures this initial instability as well as the subsequent nonlinear motion that leads to loop formation and ultimately to intertwining.

Figure 7 illustrates four representative snap-shots during the dynamic evolution of an intertwined state. The geometry just after initial buckling is approximately helical as can be observed in the uppermost snap-shot (20 seconds). Notice that the rod centerline appears to make a single helical turn as predicted from the fundamental buckling mode of the linearized theory (refer to Zachmann [26]). The superimposed black stripe records the computed twist distribution of the rod for this state which exhibits nearly four complete turns; refer to the discussion of twist and major topological transitions below. As this twist is increased, the rod continuously deforms into a larger diameter helical loop and the left end slides substantially to the right as shown by the second image (25 seconds).

Upon greater twist, the left end continues to slide towards the right end and the helical loop continues to rotate out of the plane of this figure. Eventually the loop undergoes a loss of stability followed by a rapid dynamic collapses into self-contact in forming a nearly planar loop. The collapsed loop is shown by the third image (which occurs at approximately 29 seconds).

The dynamic collapse can be anticipated from stability analyses of the equilibrium forms of a rod under similar loading conditions; refer to Lu and Perkins [27] and studies cited therein. The snap-shot at 25 seconds shows the three-dimensional shape of the rod just prior to dynamic collapse. Here, the apex of the loop has rotated approximately 90° about the vertical (e_1) axis so that the tangent at the apex is now orthogonal to the loading (e_2) axis. This was the noted secondary bifurcation condition in Lu and Perkins [27] at which the three-dimensional equilibrium form loses stability.

The collapsed loop, however, is very sensitive to the increasing twist and rapidly continues to rotate about the vertical (e_1) axis leading to intertwined forms with multiple sites of self-contact. A snapshot of a fully intertwined loop is illustrated at the bottom of Fig. 7 (32 seconds). The strain energy density (color scale in Fig. 7) reveals that the strain energy becomes highly localized to the apex of the intertwined loop where the curvature is greatest. The decomposition of this strain energy into bending and torsional components provides significant insight into the dynamic evolution of an intertwined state as discussed next.

4.3 Energetic Transitions

Figure 8 summarizes the energetics of this process by illustrating how the bending and torsional strain energy components contribute to the total strain energy. Starting at time zero, the initially straight rod remains straight and the applied twist simply increases the torsional strain energy. This elementary, pure-twisting of the straight rod ceases at approximately 18 seconds with the first bifurcation due to torsional buckling (refer to Zachmann [26]). The torsional strain energy achieves its maximum at this state and immediately thereafter the rod buckles into a three-dimensional form resembling a shallow helix (a). This transition is accompanied by a conversion of torsional to bending strain energy. This conversion is dynamic and markedly increases as the rod is twisted further while developing a distinctive loop (b). The apex of this loop rotates further out of plane during this stage. Just prior to 29 seconds the apex becomes nearly orthogonal to the loading axis (original axis of the straight rod) which marks the secondary bifurcation [27] that generates an extremely fast dynamic collapse to self-contact. The resulting loop with self-contact is nearly planar (c). During this secondary bifurcation, the rod loses both torsional and bending strain energies until self-contact and, thereafter intertwining begins. As intertwining advances (d), the torsional strain energy continues to decrease while the bending strain energy increases once more. In addition, the bending strain energy becomes localized to the apex of the loop due to the significant and increasing curvature developed there; refer also to snapshot at 32 seconds in Fig. 7. In the case of DNA forming plectonemes, such localized strain energy might possibly be the forerunner

of the nonlinear 'kinking' of the molecule as proposed recently in Wiggins et al. [28]. Figure 8 also illustrates the total strain energy and the work done by twisting the right boundary. The energy difference between the work done and the total strain energy derives from the significant kinetic energy during this process as well as the dissipation developed from the included fluid drag.

We emphasize that the results above are insensitive to any reasonable changes in the parameters in the contact law (13). Consider that the maximum dynamic contact force generated in this example is of the order of 10^{-3} N and that the corresponding contact energy density remains an order of magnitude smaller than the rod strain energy density S_e. Thus, when integrated over the length of the rod, the contribution of the contact energy remains negligible relative to the total rod strain energy. That said, for very long (hence flexible) DNA filaments with relatively large sub-domains in close proximity, the energy of self-interaction (electrostatic potential) may indeed grow to a considerable portion of the structural deformation energy of the molecule. In these instances, the equilibrium conformation of intertwined DNA would be materially affected by the electrostatic interaction.

4.4 Topological Transitions

It is interesting to observe that the topological changes for the example rod above are also exhibited by DNA during supercoiling. As discussed in Calladine et al. [1], the above conversion of torsional strain energy to bending strain energy for DNA is more frequently described topologically as the conversion of *twist* to *writhe*. We explore this

conversion in the above example after briefly reviewing the definitions for twist and writhe.

Twist (Tw) is a kinematical quantity representing the total number of twisted turns along the rod centerline as computed from

$$Tw = \frac{1}{2\pi}\int_0^{L_C} (\kappa \cdot \hat{t})ds \tag{15}$$

Writhe (Wr) is defined as the average number of cross-overs of the rod centerline when observed over all possible views of the rod (refer to Calladine et al. [1]). For our initially straight configuration, Wr = 0. At the first self-contact shown by the snapshot at 29 seconds in Fig. 7, Wr = 1. The writhe then continues to increase to Wr = 2 for the intertwined state at 32 seconds in Fig. 7. The writhe is purely a function of the space curve defining the rod centerline and it may also be positive or negative depending on whether the crossing is right-handed or left-handed (refer to Calladine et al. [1]). In our illustrative example, the sum Tw + Wr equals the number of rotations of the right boundary and this sum is called the *Linking number* Lk[2]. Refer to Fuller [29] and White [30] for the proof of conservation of the Linking number (Lk).

In our example, the initial twisting phase rapidly increases Lk from 0 to approximately 4, all in the form of twist, prior to the first bifurcation (torsional buckling) as illustrated in Fig. 9. An additional increase in Lk (end rotation) of less than ½ (turn) produces all of the

[2] This is not true, in general, for other boundary conditions that allow rotations about the other axes (i.e., cases where $\omega_{1,2} \neq 0$ at the boundaries).

sudden transitions noted above. Following the first bifurcation, Wr increases from 0 to 1 at self-contact (29 seconds) and Tw correspondingly reduces so that the sum Wr + Tw remains equal to Lk. Following the first self-contact, the loop continues to rotate as it intertwines. In doing so, every half rotation of the loop establishes an additional contact site thereby increasing Wr by 1 and reducing Tw by 1. At 32 seconds, Wr is slightly larger than 2. Thus, we observe two crossovers in any three orthogonal views of the snap-shot at 32 seconds shown in Fig. 7. There is a compensatory loss in Tw as shown in Fig. 9.

It should also be noted if self-contact is ignored, as has often been done in some prior studies of the looping of rods, the numerical solution for the rod may allow it to artificially 'cut through itself' leading to entirely different and non-physical results. Following each 'cut', both Wr and Lk are reduced discontinuously by 2. Examples of this readily follow from the present computational formulation by simply eliminating the contact force. However, doing so leads to non-physical discontinuous changes in Wr and Lk following artificial 'cuts' through the rod. Thus, modeling self-contact is fundamentally necessary when one endeavors to understand the pathway(s) leading to the intertwined loops.

5. CONCLUSIONS

This paper summarizes a computational rod model that captures the dynamical evolution of intertwined loops in rods under torsion. A major feature is the explicit formulation of

dynamic self-contact. An illustrative example is selected which reveals a fundamental understanding of how loops first form, then collapse, and then intertwine. This knowledge may also promote an understanding of how long cables form 'hockles' and how DNA molecules form plectonemic supercoils.

Numerical simulations reveal that an originally straight rod undergoes two bifurcations in succession as twist is added. The first bifurcation is elementary and occurs at the (Zachmann) buckling condition where the trivial equilibrium becomes unstable and the rod buckles into the approximate shape of a shallow helix. Upon increasing twist, this helix grows in amplitude to form a distinctive loop. In doing so, the apex of this loop continues to rotate towards the out-of-plane direction. When the apex ultimately becomes orthogonal to the loading axis (axis of the original straight rod), the loop experiences a secondary bifurcation and a sudden dynamic collapse into a near-planar loop with self-contact. As twist is again added, the near-planar loop rotates upon itself becoming intertwined with multiple sites of self-contact. The energetics leading to the intertwined form confirm the large exchange of torsional strain energy for bending strain energy which becomes increasingly localized to the apex of the loop. These transitions parallel the dynamic conversion of twist (Tw) to writhe (Wr) during this process.

ACKNOWLEDGEMENTS

The authors (NCP and SG) gratefully acknowledge the research support provided by the U.S. Office of Naval Research (grant N00014-00-1-0001), the Lawrence Livermore

National Laboratories (grant B 531085), and the U. S. National Science Foundation (grants CMS 0439574 and CMS 0510266). The author (CLL) performed work under the auspices of the U.S. Department of Energy by the University of California, Lawrence Livermore National Laboratory under contract No.W-7405-ENG-48.

REFERENCES

1. C.R. Calladine, H.R. Drew, B.F. Luisi and A.A. Travers, *Understanding DNA, the molecule and how it works*, 3rd edition. Elsevier Academic Press, Amsterdam (2004).
2. S. Goyal, T. Lillian, N.C. Perkins and E. Meyhofer, Cable dynamics applied to long-length scale mechanics of DNA. *in CD-ROM Proceedings of Sixth International Symposium of Cable Dynamics*, Chaleston, South Carolina (2005).
3. C. Branden and J. Tooze, *Introduction to protein structure*, 2nd edition. Garland Publishing, New York (1999).
4. A.L. Lehninger, D.L. Nelson and M.M. Cox, *Lehninger principles of biochenistry*, 4th edition. W.H. Freeman, New York (2005).
5. R. Schleif, DNA looping. *Annu. Rev. Biochem.* **61**, 199 (1992).
6. S. Semsey, K. Virnik and S. Adhya, A gamut of loops: Meandering DNA. *Trends Biochem. Sci.* **30**(6), 334 (2005).
7. S. Goyal, A dynamic rod model to simulate mechanics of cables and DNA.*Ph.D. Dissertation in Mechanical Engineering*, *University of Michigan, Ann Arbor* (2006).
8. N. Chouaieb, A. Goriely and J.H. Maddocks, Helices. *Proc. Natl. Acad. Sci. U.S.A.* **103**(25), 9398 (2006).
9. G.H.M. van der Heijden, M.A. Peletier and R. Planque, Self-contact for rods on cylinders. *Arch. Ration. Mech. and Anal.* **182**(3), 471 (2006).
10. F. Schuricht and H. von der Mosel, Euler-lagrange equations for nonlinearly elastic rods with self-contact. *Arch. Ration. Mech. and Anal.* **168**(1), 35 (2003).
11. G.H.M. van der Heijden, S. Neukirch, V.G.A. Goss and J.M.T. Thompson, Instability and self-contact phenomena in the writhing of clamped rods. *Int. J. Mech. Sci.* **45**(1), 161 (2003).
12. B.D. Coleman, D. Swigon and I. Tobias, Elastic stability of DNA configurations. II. Supercoiled plasmids with self-contact. *Phys. Rev. E* **61**(1), 759 (2000).
13. O. Gonzalez, J.H. Maddocks, F. Schuricht and H. von der Mosel, Global curvature and self-contact of nonlinearly elastic curves and rods. *Calculus of Variations and Partial Differential Equations* **14**(1), 29 (2002).
14. B.D. Coleman and D. Swigon, Theory of self-contact in kirchhoff rods with applications to supercoiling of knotted and unknotted DNA plasmids. *Phil. Trans. Roy. Soc. Lond. A* **362**(1820), 1281 (2004).
15. B.D. Coleman and D. Swigon, Theory of supercoiled elastic rings with self-contact and its application to DNA plasmids. *J. Elasticity* **60**(3), 173 (2000).
16. B.D. Coleman and D. Swigon, Theory of self-contact in DNA molecules modeled as elastic rods. *Nuovi progressi nella fisica matematica dall'eredità di Dario Graffi* **177**, 281 (2002).

17. S. Goyal, N.C. Perkins and C.L. Lee, Writhing dynamics of cables with self-contact. *in Proceedings of Fifth International Symposium of Cable Dynamics*, Santa Margherita Ligure, Italy, 27 (2003).
18. I. Klapper, Biological applications of the dynamics of twisted elastic rods. *J. Comput. Phys.* **125**(2), 325 (1996).
19. A.E.H. Love, *A treatise on the mathematical theory of elasticity*, 4th edition. Dover Publications, New York (1944).
20. D.T. Greenwood, *Principles of dynamics*, 2nd edition. Prentice-Hall, Englewood Cliffs, N.J. (1988).
21. S. Goyal, N.C. Perkins and C.L. Lee, Nonlinear dynamics and loop formation in kirchhoff rods with implications to the mechanics of DNA and cables. *J. Comput. Phys.* **209**(1), 371 (2005).
22. J. Chung and G.M. Hulbert, A time integration algorithm for structural dynamics with improved numerical dissipation - the generalized-alpha method. *ASME J. Appl. Mech.* **60**(2), 371 (1993).
23. T. Schlick, W.K. Olson, T. Westcott and J.P. Greenberg, On higher buckling transitions in supercoiled DNA. *Biopolymers* **34**(5), 565 (1994).
24. T. Schlick, B. Li and W.K. Olson, The influence of salt on the structure and energetics of supercoiled DNA. *Biophys. J.* **67**(6), 2146 (1994).
25. J.R. Morison, M.P. Obrien, J.W. Johnson and S.A. Schaaf, The force exerted by surface waves on piles. *Trans. Am. Inst. Min. Metall. Eng.* **189**, 149 (1950).
26. D.W. Zachmann, Non-linear analysis of a twisted axially loaded elastic rod. *Quart. Appl. Math.* **37**(1), 67 (1979).
27. C.L. Lu and N.C. Perkins, Nonlinear spatial equilibria and stability of cables under uniaxial torque and thrust. *ASME J. Appl. Mech.* **61**(4), 879 (1994).
28. P.A. Wiggins, R. Phillips and P.C. Nelson, Exact theory of kinkable elastic polymers. *Phys. Rev. E* **71**(2), (2005).
29. F.B. Fuller, Writhing number of a space curve. *Proc. Natl. Acad. Sci. U.S.A.* **68**(4), 815 (1971).
30. J.H. White, Self-linking and gauss-integral in higher dimensions. *Am. J. Math.* **91**(3), 693 (1969).

quantity	***units (SI)***	***value/ formula***
Young's Modulus, E	Pa	1.25×10^{7}
Shear Modulus, G	Pa	5.0×10^{6}
Diameter, D	m	See Fig. 5
Length, L_c	m	1.0
Rod Density, ρ_c	Kg/m^3	1500
Fluid Density, ρ_f	Kg/m^3	1000
Normal Drag Coefficient C_n	-	0.1
Tangential Drag Coefficient C_t	-	0.01
Temporal Step, Δt	s	0.1
Spatial Step, Δs	m	0.001
Cross-section Area	m^2	$A_c = \frac{\pi D^2}{4}$
Mass/ length	Kg/m	$m = \rho_c A_c$
Area Moments of Inertia (bending)	m^4	$J_{1,2} = \frac{A_c D^2}{16}$
Area Moment of Inertia (torsion)	m^4	$J_3 = \frac{A_c D^2}{8}$
Mass Moment of Inertia/ length	Kg-m	$I = \rho_c J$

Table 1: Example rod properties and simulation parameters.

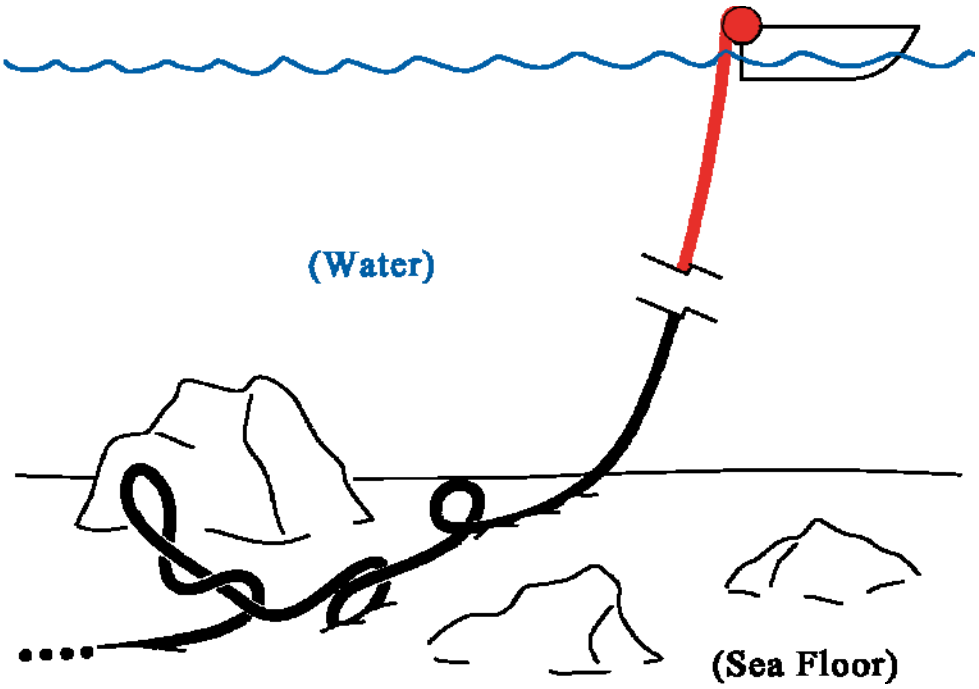

Figure 1: Low tension cable forming loops and (intertwined) tangles on the sea floor.

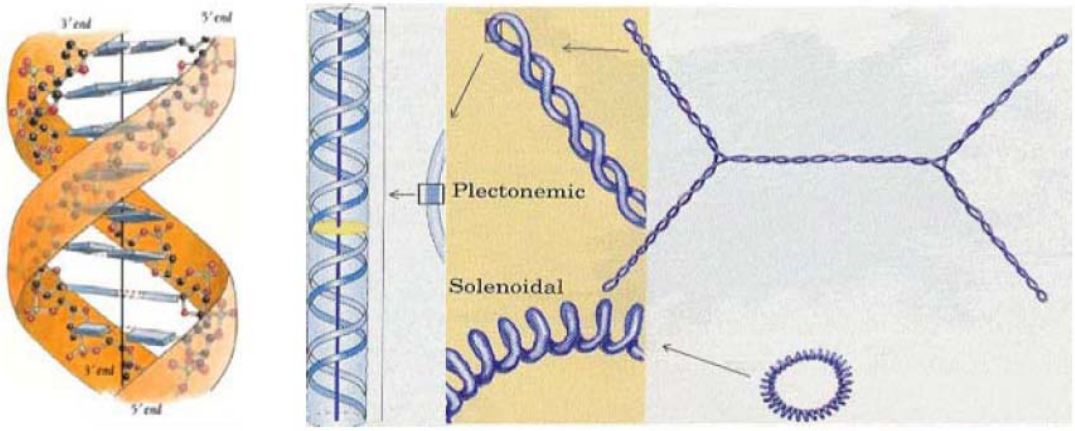

Figure 2: DNA shown on three length scales. Smallest scale (left) shows a single helical repeat of the double-helix structure (sugar-phosphate chains and base-pairs). Intermediate scale (middle) suggests how many consecutive helical repeats form the very long and slender DNA molecule. Largest scale (right) shows how the molecule ultimately curves and twists in forming supercoils (plectonemic or solenoidal). (Courtesy: Branden and Tooze [3] and Lehninger et al. [4]).

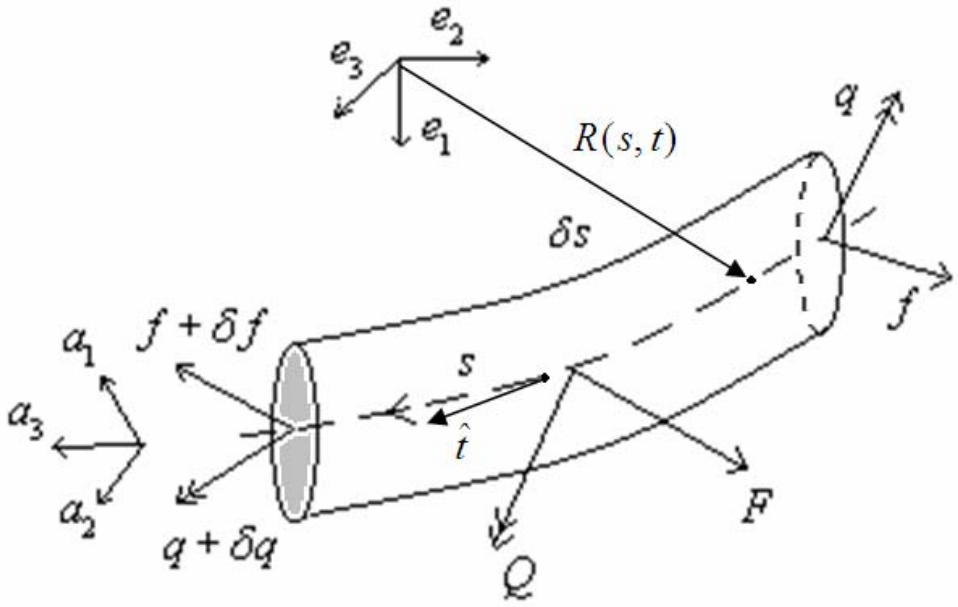

Figure 3: Free body diagram of an infinitesimal element of a Kirchhoff rod.

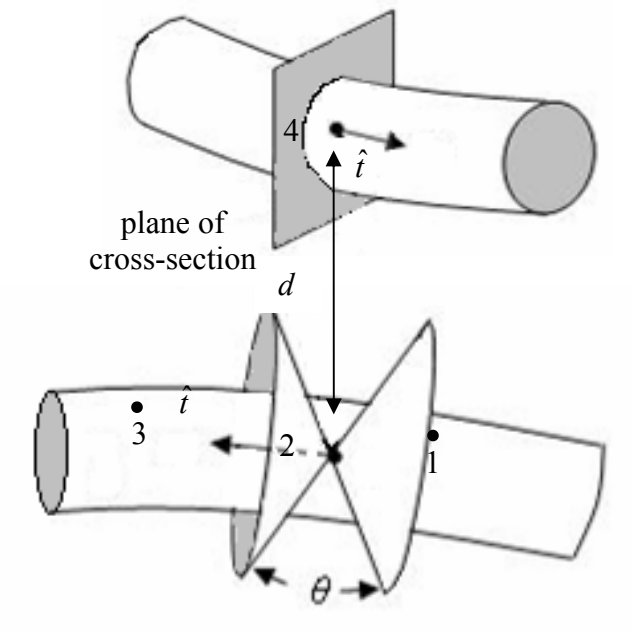

Figure 4: Two remote segments of a rod approaching contact. A *screening aperture* is defined by a pair of conical surfaces constructed at each grid point. This aperture leads to an efficient numerical search for regions of self-contact.

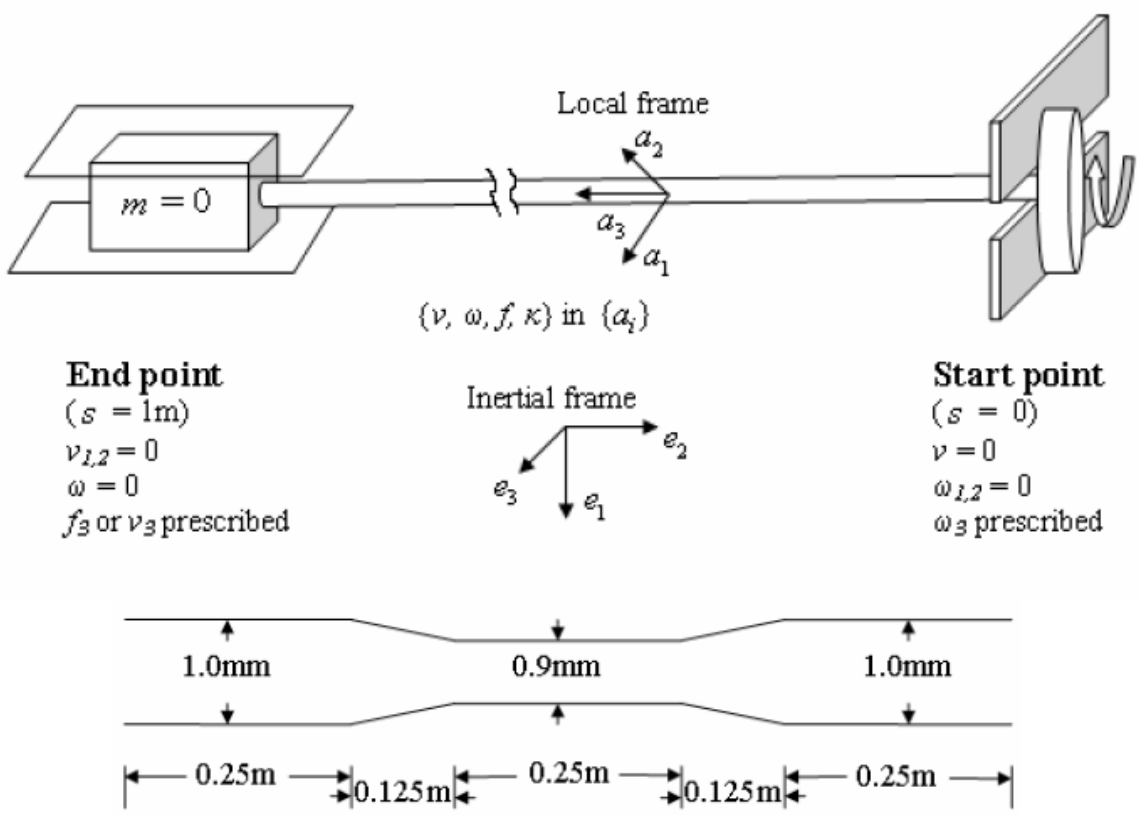

Figure 5: A non-homogenous rod subject to slowly increasing twist created by rotating the right end about the e_2 (loading) axis The right end is otherwise restrained in rotation and translation. The left end is fully restrained in rotation and translation except that it is free to slide along the loading axis.

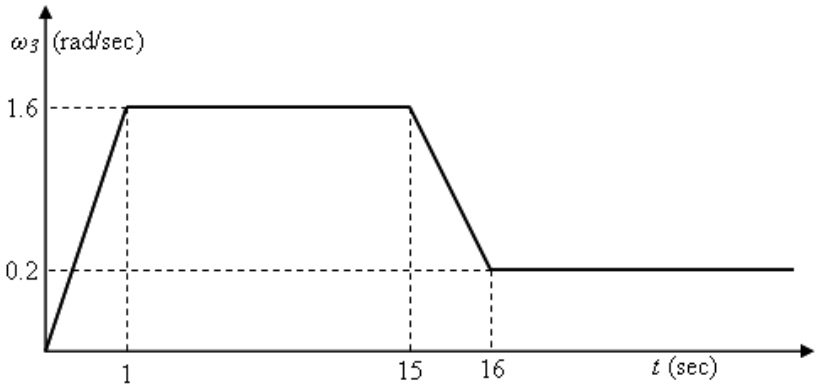

Figure 6: Prescribed angular (twist) velocity at the right end. (Note: not to scale).

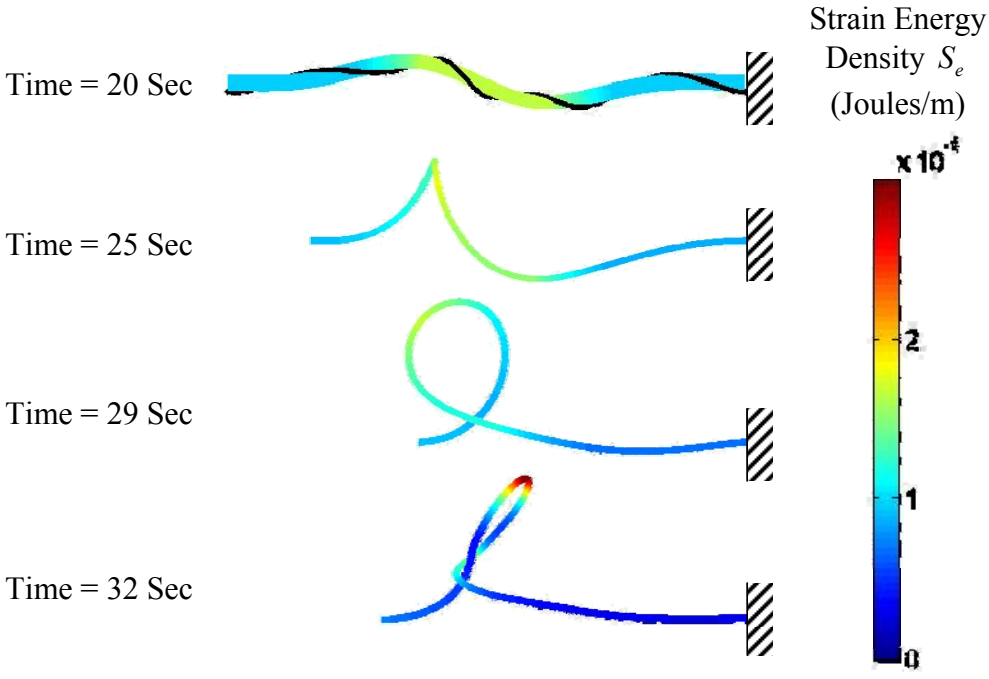

Figure 7: Snap-shots at selected times during the transition from a buckled helical form (Time=20 sec.) to an intertwined form (Time=32 sec.). Black stripe superimposed on the first form illustrates the twist distribution. Color indicates strain energy density.

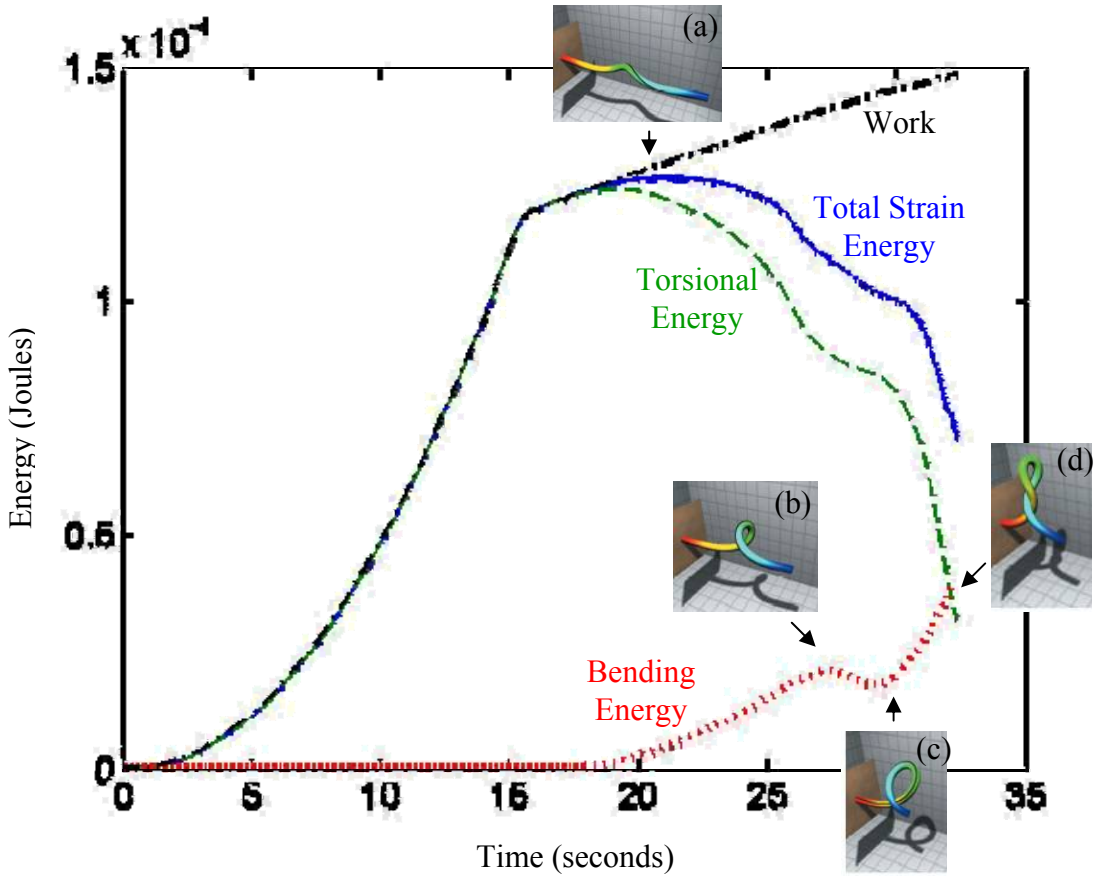

Figure 8: The bending, torsional, and total strain energy during the dynamic evolution of an intertwined state. The work done by the applied twist is also reported.

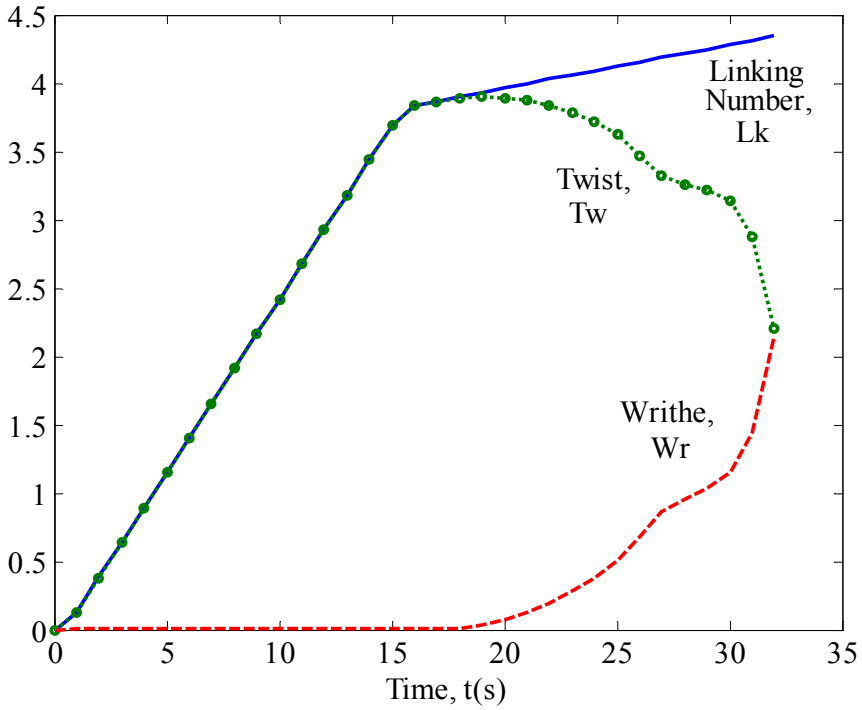

Figure 9: Conversion of twist (Tw) to writhe (Wr) during loop formation and intertwining. The linking number Lk = Tw + Wr is equivalent to the number of turns prescribed at the right end of the rod in this example.